ADVANCED MATERIALS
www.advmat.de

Colossal Strain Tuning of Ferroelectric Transitions in $KNbO_3$ Thin Films

*Sankalpa Hazra, Tobias Schwaigert, Aiden Ross, Haidong Lu, Utkarsh Saha, Victor Trinquet, Betul Akkopru-Akgun, Benjamin Z. Gregory, Anudeep Mangu, Suchismita Sarker, Tatiana Kuznetsova, Saugata Sarker, Xin Li, Matthew R. Barone, Xiaoshan Xu, John W. Freeland, Roman Engel-Herbert, Aaron M. Lindenberg, Andrej Singer, Susan Trolier-McKinstry, David A. Muller, Gian-Marco Rignanese, Salva Salmani-Rezaie, Vladimir A. Stoica, Alexei Gruverman, Long-Qing Chen, Darrell G. Schlom, and Venkatraman Gopalan**

Strong coupling between polarization (P) and strain (ε) in ferroelectric complex oxides offers unique opportunities to dramatically tune their properties. Here colossal strain tuning of ferroelectricity in epitaxial $KNbO_3$ thin films grown by sub-oxide molecular beam epitaxy is demonstrated. While bulk $KNbO_3$ exhibits three ferroelectric transitions and a Curie temperature (T_c) of ≈676 K, phase-field modeling predicts that a biaxial strain of as little as −0.6% pushes its T_c > 975 K, its decomposition temperature in air, and for −1.4% strain, to T_c > 1325 K, its melting point. Furthermore, a strain of −1.5% can stabilize a single phase throughout the entire temperature range of its stability. A combination of temperature-dependent second harmonic generation measurements, synchrotron-based X-ray reciprocal space mapping, ferroelectric measurements, and transmission electron microscopy reveal a single tetragonal phase from 10 K to 975 K, an enhancement of ≈46% in the tetragonal phase remanent polarization (P_r), and a ≈200% enhancement in its optical second harmonic generation coefficients over bulk values. These properties in a lead-free system, but with properties comparable or superior to lead-based systems, make it an attractive candidate for applications ranging from high-temperature ferroelectric memory to cryogenic temperature quantum computing.

1. Introduction

The ability to apply large strains in epitaxial thin films makes it possible to engineer emergent phases in materials with enhanced material properties that are inaccessible in their bulk form.[1] Owing to a strong coupling between strain and polar order in ferroelectrics, large shifts in properties such as paraelectric-to-ferroelectric transition temperature (T_c) and remanent polarization (P_r) have been theoretically predicted and experimentally observed.[2–6] Notable examples of strain-enhanced properties and tunable phase transitions in perovskite oxides include a large shift in T_c in $BaTiO_3$,[2] observation of room temperature ferroelectricity in quantum paraelectric $SrTiO_3$,[3,4] and the realization of supertetragonal $BiFeO_3$.[7] Given that there are practical limits to epitaxially straining a ceramic thin film on a rigid single crystal substrate to typically a few percent (a maximum

S. Hazra, A. Ross, U. Saha, B. Akkopru-Akgun, T. Kuznetsova, S. Sarker, S. Trolier-McKinstry, V. A. Stoica, L.-Q. Chen, V. Gopalan
Department of Materials Science and Engineering
Pennsylvania State University
University Park, PA 16802, USA
E-mail: vgopalan@psu.edu

The ORCID identification number(s) for the author(s) of this article can be found under https://doi.org/10.1002/adma.202408664

DOI: 10.1002/adma.202408664

T. Schwaigert, M. R. Barone
Platform for the Accelerated Realization, Analysis, and Discovery of Interface Materials (PARADIM)
Cornell University
Ithaca, NY 14853, USA

T. Schwaigert, M. R. Barone, A. Singer, D. G. Schlom
Department of Materials Science and Engineering
Cornell University
Ithaca, NY 14853, USA

H. Lu, X. Li, X. Xu, A. Gruverman
Department of Physics and Astronomy
University of Nebraska
Lincoln, NE 68588, USA

of 6.6% has been demonstrated[7]), one ideally desires the maximum strain *tunability* of the film properties, measured in units of property per unit strain, such as $\frac{dT_c}{d\varepsilon}$ and $\frac{dP_r}{d\varepsilon}$.

Moreover, to achieve the desired phase over a broad temperature range, undesirable thermal phase transitions require suppression. For instance, in $BaTiO_3$-based electrooptic modulators employed in quantum computing at cryogenic temperatures, symmetry-lowering phase transitions in $BaTiO_3$ significantly diminish the superior electrooptic properties of the room-temperature tetragonal phase.[8] Stabilization of the tetragonal phase in this system at cryogenic operational temperatures would thus be ideal. For high-temperature ferroelectric memory and actuation applications, the stabilization of ferroelectricity at high temperatures through a large T_c is desired. Further, environmentally benign ferroelectrics[9,10] are desired, in contrast to Pb-based ferroelectrics.

Strain tuning of environmentally benign perovskite alkali niobates have been explored due to their strong ferroelectricity,[11] piezoelectricity,[12,13] and nonlinear optical responses.[14] In $(Na,K)NbO_3$ films, strain tuning proves to be an effective pathway to control phase transitions,[15,16] while allowing properties competing with those of Pb-based ferroelectrics.[17] Unfortunately, $NaNbO_3$ is highly polymorphic as compared with $KNbO_3$, making pure $KNbO_3$ a more suitable material system to establish a single structural phase across a large temperature range.[18] While strain-relaxed $KNbO_3$ films have been studied,[19–24] strain tuning of this Pb-free, environmentally benign system has not been explored thus far. Furthermore, prior demonstrations of the growth of $KNbO_3$ on a silicon substrate[25,26] make $KNbO_3$ appealing for semiconductor device integration.

In this work, we demonstrate that strain-tuning of $KNbO_3$ provides a colossal strain tunability of its T_c, while retaining the desirable tetragonal phase from 10 K to 975 K, its decomposition temperature in air. Strain mediates the stabilization of a superior tetragonal phase in $KNbO_3$, mimicking the tetragonality of $PbTiO_3$ but with much higher T_c, and significantly larger nonlinear optical coefficients.

2. Theory Prediction of the Strain Phase Diagram

Bulk $KNbO_3$ has a rich phase diagram undergoing a series of phase transitions from cubic to tetragonal at 676 K, tetragonal to orthorhombic at 492 K, and eventually orthorhombic to rhombohedral at 223 K.[11] To predict the influence of biaxial strain on the lattice parameters and temperature-dependent phase diagram of $KNbO_3$, we performed phase-field simulations of biaxially compressed $KNbO_3$ thin films.

Figure 1a depicts the phase diagram predicted from phase-field simulations as a function of biaxial epitaxial strain, $\varepsilon = (a_{||} - a_o)/a_o$, where a_o is the effective cubic lattice parameter extrapolated from the high-temperature $KNbO_3$ cubic phase and $a_{||}$ is the in-plane lattice parameter of the biaxially strained $KNbO_3$. Under a compressive strain of $\approx -0.7\%$, it is possible to stabilize the high-temperature tetragonal phase at room temperature where the orthorhombic phase is observed in its bulk counterpart. Further, a strain of $\approx -1.5\%$ is sufficient to stabilize the tetragonal phase down to 0 K, eliminating all other phase transitions. At such strains, the Curie temperature, T_c is predicted to be enhanced beyond its melting temperature of 1325 K[18] as seen in Figure 1a. Strikingly, the rate of change of T_c with respect to strain, i.e., $\frac{dT_c}{d\varepsilon}$, is predicted to be a factor of $\approx 3\times$ higher compared to most well-known ferroelectrics as shown in Figure 1b, while its rate of change of remanent polarization with respect to strain, $\frac{dP_r}{d\varepsilon}$, is predicted to be intermediate between that of tetragonal $BiFeO_3$[27] and $PbZr_{0.3}Ti_{0.7}O_3$.[28]

The superior stability of the tetragonal phase under higher compressive strains is driven by its better match with strain conditions imposed by the substrate, resulting in minimal elastic energy in comparison to other possible phases. For lower compressive strains, $KNbO_3$ is predicted to undergo a transition from the tetragonal to a lower symmetry monoclinic phase instead of an orthorhombic phase as seen in bulk $KNbO_3$. This is because of the large enhancement of the c/a lattice parameter ratio (Figure 1c) due to the epitaxial clamping to the substrate, effectively distorting the orthorhombic phase in bulk $KNbO_3$ into a monoclinic phase under compressive strain (see Supporting Information). At room temperature, the c/a ratio increases from its bulk value of ≈ 1.01 (similar to that of bulk $BaTiO_3$) to a value of ≈ 1.07 (larger

V. Trinquet, G.-M. Rignanese
Institute of Condensed Matter and Nanosciences
UCLouvain
Louvain-la-Neuve 1348, Belgium

B. Z. Gregory
Department of Physics
Cornell University
Ithaca, NY 14853, USA

A. Mangu, A. M. Lindenberg
Department of Materials Science and Engineering
Stanford University
Stanford, CA 94305, USA

A. Mangu, A. M. Lindenberg
Stanford Institute for Materials Energy Sciences
SLAC National Accelerator Laboratory
Menlo Park, CA 94025, USA

S. Sarker
Cornell High Energy Synchrotron Source
Cornell University
Ithaca, NY 14853, USA

J. W. Freeland
Advanced Photon Source
Argonne National Laboratory
Argonne, IL 60439, USA

R. Engel-Herbert
Paul-Drude-Institut für Festkörperelektronik
Leibniz-Institut im Forschungsverbund Berlin e.V.
Hausvogteiplatz 5, 10117 Berlin, Germany

D. A. Muller
School of Applied and Engineering Physics
Cornell University
Ithaca, NY 14853, USA

S. Salmani-Rezaie
Department of Materials Science and Engineering
Ohio State University
Columbus, OH 43210, USA

S. Salmani-Rezaie, D. G. Schlom
Kavli Institute at Cornell for Nanoscale Science
Ithaca, NY 14853, USA

D. G. Schlom
Leibniz-Institut für Kristallzüchtung
Max-Born-Straße 2, 12489 Berlin, Germany

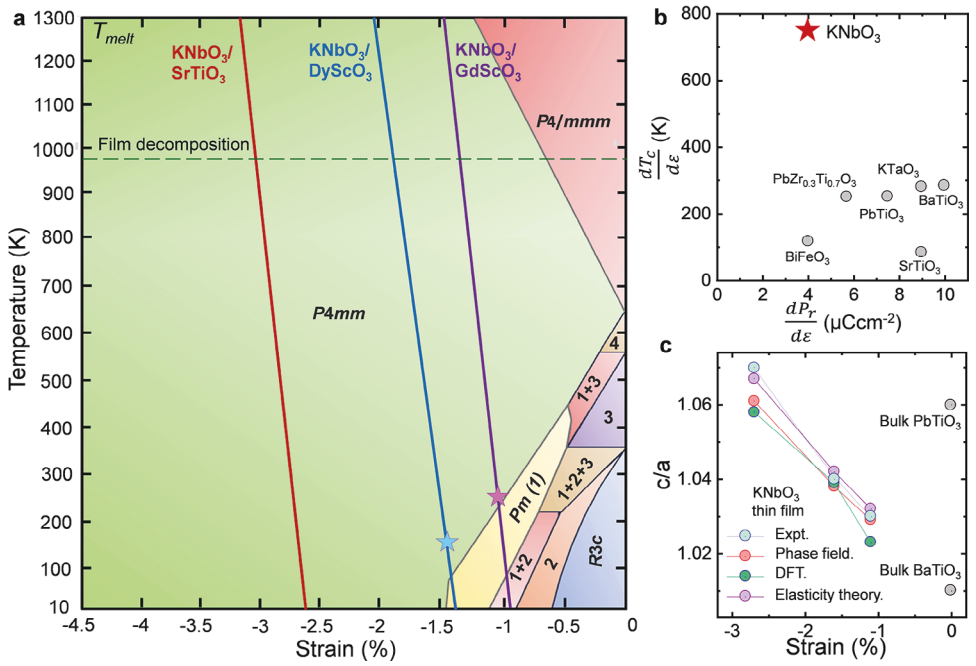

Figure 1. a) Thermodynamic phase-field simulations of biaxially compressed $KNbO_3$. The three different strain films on $SrTiO_3$, $DyScO_3$, and $GdScO_3$ studied here are marked by red, blue, and violet lines. Legend for numerically labeled phases: 1: *Pm*, 2: *Cm*, 3: *Amm*2, 4: Phase mixture of *P*4*mm* with *c*-axis poled in the in-plane direction and out-of-plane direction. Blue and violet stars indicate the onset of the tetragonal-to-monoclinic transition temperature observed experimentally. b) $\frac{dT_c}{d\varepsilon}$ and $\frac{dP_r}{d\varepsilon}$ plotted for $KNbO_3$ in comparison to related materials: $BaTiO_3$,[27,75] $PbTiO_3$,[1,27,76] $PbZr_{0.3}Ti_{0.7}O_3$,[28,77] $SrTiO_3$,[3,78] $KTaO_3$,[79,80] and $BiFeO_3$.[7,27,81] $\frac{dT_c}{d\varepsilon}$ for $KNbO_3$ is labeled by predicted values from phase-field simulations. c) *c*/*a* ratio (out-of-plane to in-plane lattice parameter ratio) plotted as a function of strain experimentally measured for $KNbO_3$ thin films at room temperature compared to phase-field predictions, DFT calculations, and elasticity theory calculations (see Supporting information), showing the effect of strain in enhancing the stability of the tetragonal phase in $KNbO_3$.

than that for bulk $PbTiO_3$) at −2.7% strain. The polarization direction and lattice structure of the strain-stabilized tetragonal and monoclinic phases in the $KNbO_3$ thin films are shown in Figure S1 (Supporting Information).

Density functional theory calculations also predict the stability of the monoclinic phase to be comparable to the tetragonal phase for intermediate strains (Figure S2, Supporting Information). From finite-temperature phase-field simulations, it is evident that for higher compressive strains (more than ≈ −1.5%) all symmetry-lowering phase transitions can be eliminated and the single desirable tetragonal phase can be stabilized across the entire temperature regime from 0 K to T_c.

From thermodynamic calculations, the Curie temperature, T_c, for the tetragonal *c*-phase under a biaxial compressive strain (*c*-axis perpendicular to the substrate) is given by,

$$T_c(\varepsilon) = T_c(\varepsilon = 0) + 4\varepsilon_o C\left(\frac{Q_{13}}{S_{11}+S_{13}}\right)|\varepsilon| \quad (1)$$

where C is the Curie–Weiss constant, Q is the electrostrictive coefficient, S is the elastic compliance, and ε_o is the vacuum permittivity. Comparing the C, Q, and S of $KNbO_3$ versus those for $PbTiO_3$, $BaTiO_3$, and $SrTiO_3$, (Table S3 Supporting Information) it is evident that the strong sensitivity of T_c to strain is predominantly due to a larger electrostrictive coefficient, Q_{13}, in $KNbO_3$. For example, C, $\frac{1}{S_{11}+S_{13}}$, and Q_{13} are ≈6%, ≈40%, and ≈200% larger in $KNbO_3$ relative to $PbTiO_3$, thus leading to a ≈3 × larger $\frac{dT_c}{d\varepsilon}$.

Following Equation (1), it is evident that a larger Q_{13} and lower $S_{11} + S_{13}$ translates to a higher T_c and $\frac{dT_c}{d\varepsilon}$. Unfortunately, this linear relationship does not extend to the case of P_r and $\frac{dP_r}{d\varepsilon}$, where there are optimal values for Q and S which maximize P_r and $\frac{dP_r}{d\varepsilon}$, as shown in Figure S3 (Supporting Information). In particular, the Q_{13} and $S_{11} + S_{13}$ values of $KNbO_3$ do not optimize the maximum possible value of P_r and $\frac{dP_r}{d\varepsilon}$; nonetheless these values are highly competitive with other material systems as shown in Figure 1b.

3. Epitaxy and Phase Transitions by Optical Second Harmonic Generation

To experimentally measure the strain phase diagram, single crystal $(001)_c$ $SrTiO_3$, $(110)_o$ $DyScO_3$, and $(110)_o$ $GdScO_3$ (subscript "c" for cubic, "o" for orthorhombic) were used as compatible substrates, which allows us to impart compressive strain, ε, of ≈−2.7%, −1.6%, and −1.1%, respectively, on (001) $KNbO_3$ films. (To be precise, the biaxial in-plane strain for the scandate substrates is anisotropic, namely −1.65% and −1.5% for $DyScO_3$, and −1.15% and −1.05% for $GdScO_3$. Note that this difference was not experimentally resolved and is hence ignored in the rest of this study). Epitaxial $KNbO_3$ thin films were grown by suboxide molecular-beam epitaxy with in situ reflection high-energy

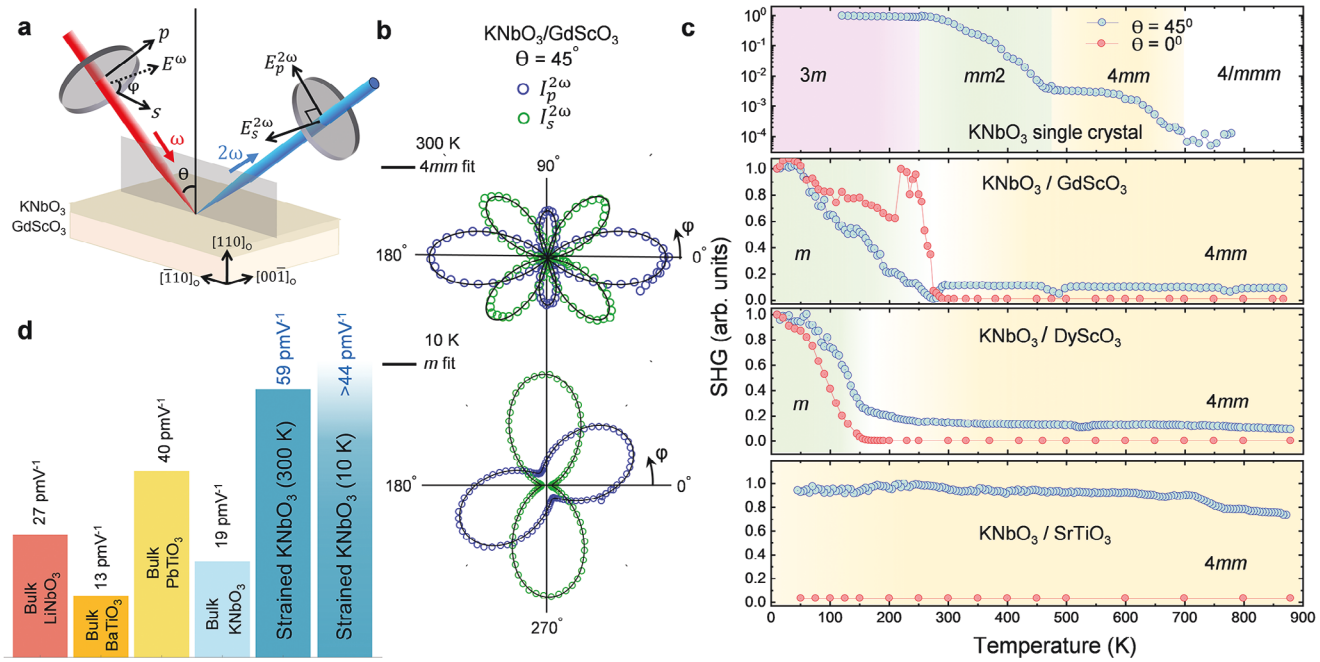

Figure 2. a) Schematic of second harmonic generation (SHG) setup in reflection geometry. b) SHG polar plots for $KNbO_3$ on $GdScO_3$ at 300 K (upper panel) and 10 K (lower panel) fitted to tetragonal and multidomain monoclinic models, respectively, showing symmetry lowering from room temperature to low temperature consistent with phase-field predictions. Equations for SHG modeling are discussed in the Supporting information. c) Normal and oblique-incidence SHG intensity versus temperature between 10 K and 900 K shown for bulk $KNbO_3$ single crystal, and strained $KNbO_3$ films on $GdScO_3$, $DyScO_3$, and $SrTiO_3$ substrates. Bulk phase transition temperatures are consistent with previous reports. Normal-incidence SHG signal (red traces) shows signatures of transition from tetragonal to a lower symmetry monoclinic phase since it is sensitive only to the latter phase. With increasing compressive strain, this symmetry-lowering phase transition (marked by green regions) is pushed down in temperature and eventually eliminated in the highest strained $KNbO_3$ on $SrTiO_3$. d) Nonlinear optical coefficients (d_{33}) calculated from SHG modeling for $KNbO_3$ thin films for both 300 K and 10 K compared to bulk room temperature values in similar materials. Due to the multidomain model for the low temperature monoclinic phase, only a lower bound for the d_{11} monoclinic coefficient could be extracted.

electron diffraction (RHEED) (Figure S4, Supporting information). Atomic force microscopy (AFM) was used to confirm smooth surface morphology with root-mean-square (rms) roughness < 1 nm for all three films (Figure S5, Supporting information). X-ray reciprocal space mapping (RSM) confirms the commensurately strained nature of the thin films on all three substrates (Figures S6 and S7, Supporting information). Cross-sectional transmission electron microscopy shows a uniform interface structure with minimum interface intermixing, with the film being coherently strained to the substrate with no extended defects (Figures S8–S11 Supporting information). X-ray photoemission spectroscopy confirms the expected valence states of K, Nb, and O in $KNbO_3$ films (Figure S12, Supporting Information).

To experimentally identify the phase diagram of the strained $KNbO_3$ thin films, temperature-dependent second harmonic generation (SHG) measurements were performed. Electric-dipole SHG is a nonlinear optical process where incident light at the fundamental frequency of ω is converted into the SHG frequency of 2ω due to the broken inversion symmetry in the material.[29] A schematic of the setup used for SHG measurements is shown in **Figure** 2a. By rotating the incident polarization of light at the fundamental frequency, SHG polar plots can be measured corresponding to two orthogonally polarized (*s* and *p*-polarized) second harmonic light reflected from the sample surface; this is called SHG polarimetry. By fitting the polar plots, the point group symmetry of the thin films can be determined.

Figure 2b shows the oblique incidence SHG polarimetry for the $KNbO_3$ on $GdScO_3$ film (lowest biaxial strain, $\varepsilon \approx -1.1\%$) at 300 K fitted to a 4*mm* (tetragonal) model (see Supporting information), validating the influence of the strain in stabilizing a tetragonal phase of $KNbO_3$ at room temperature even for the lowest strained thin film of the set. A tetragonal unit cell with polarization completely out-of-plane will exhibit no SHG signal at normal incidence. Nonetheless, symmetry lowering from a tetragonal to a lower symmetry phase will generate SHG at normal incidence due to the appearance of an in-plane polarization component in lower symmetry phases. Temperature-dependent SHG at normal incidence indeed shows that $KNbO_3$ on $GdScO_3$ undergoes critical behavior ≈275 K, below which a non-zero SHG intensity is observed in this geometry (Figure 2c). In oblique incidence, the SHG intensity increases below ≈275 K reaching 10 × the room temperature intensity at 10 K. Following phase-field predictions, the low-temperature SHG polarimetry can be fitted to a multidomain monoclinic *m* model (see Supporting information), shown in the lower panel of Figure 2b for $KNbO_3$ on $GdScO_3$ at 10 K. Note that a multidomain orthorhombic *mm*2 symmetry can also be used to fit the polar plots at low-temperature. Hence, to conclusively determine the symmetry of the low-temperature phase, complementary temperature-dependent x-ray diffraction studies are necessary as discussed in Section 4.

The phase transition from tetragonal to a lower symmetry phase is further suppressed to ≈150 K for the $KNbO_3$ on $DyScO_3$ film ($\varepsilon \approx -1.6\%$), while for the highest strained $KNbO_3$ on $SrTiO_3$ ($\varepsilon \approx -2.7\%$), the low-temperature phase is completely absent, as evidenced from the temperature-dependence of normal and oblique incidence SHG amplitude as well as from the SHG polarimetry for both films (Figures S13 and S14, Supporting information). The observed phase transition temperatures are consistent with phase-field predictions and reflect the influence of strain in favoring a tetragonal phase in $KNbO_3$. Furthermore, it is noteworthy that the rhombohedral phase which appears in bulk $KNbO_3$ below 225 K is completely suppressed in all these films, even for the lowest strained sample on $GdScO_3$.

On the high-temperature end, the strain-stabilized tetragonal phase persists on heating up until 900 K for all three films, with no appreciable change in the measured SHG intensity. This suggests the robustness of the tetragonal phase. To test the highest operating temperature possible for the $KNbO_3$ films, a $KNbO_3$ film on $GdScO_3$ was heated in air to temperatures higher than the film growth temperature (≈925 K). The film shows signs of decomposition evidenced by the declining SHG intensity when heated beyond ≈975 K, while still maintaining a tetragonal symmetry that persists when cooled back down to room temperature (Figure S15, Supporting Information).

By benchmarking the SHG polarimetry to a reference sample, nonlinear optical coefficients are derived using the #SHAARP.*ml* package,[30,31] and is discussed in further detail in Supporting Information. The measured d_{33} coefficient in strained tetragonal $KNbO_3$ is shown in Figure 2d in reference to other similar ferroelectrics, reflecting a ≈200% enhancement of the d_{33} coefficient as compared to the bulk $KNbO_3$ values while ≈50% higher than bulk $PbTiO_3$ values.[32] Since at low temperatures, the films have multiple domains, extracting the full SHG tensor at low temperatures is challenging. From multi-domain modeling however, only a domain area-fraction scaled $d_{11}d$ coefficient can be estimated which is ≈44 pm V^{-1} at 10 K. Since the domain area-fraction is strictly less than 1, this value should be considered only as a lower bound estimate of the low-temperature d_{11} coefficient, i.e., $d_{11} \geq$ 44 pm V^{-1}.

4. Structural Characterization by X-Ray Diffraction

To elucidate the structural phase transition to a lower symmetry phase upon cooling, the temperature-dependent out-of-plane lattice parameter was measured for the $KNbO_3$ thin film grown on $GdScO_3$; this is the film with the lowest strain (−1.1%). As shown in **Figure 3a** the $KNbO_3$ film undergoes a change in its thermal expansion coefficient at 275 K, as extracted from the slope of lattice parameter variation versus temperature. This observation points to a film structure change that agrees with the SHG observations of the symmetry lowering at the same temperature of 275 K.

Additional 3D RSMs were obtained by synchrotron X-ray diffraction that shed more light on the nature of these observations. Diffraction images were collected with a large area detector with an incident X-ray photon energy of 50 keV, which allows sampling large reciprocal space volumes extending from 0 to 6.5 $Å^{-1}$ in the out-of-plane direction and from −5 to 5 $Å^{-1}$ in the in-plane direction. In this configuration, the RSM measurements covered several peaks that are compared to each other to suggest a domain-averaged tetragonal structure for the $KNbO_3$ film (Figure S16, Supporting information). Unfortunately, the symmetry of the film structure may remain hidden in the domain-averaged measurements. For this reason, the diffuse scattering patterns around selected peaks are more closely inspected that provide added information about the domain arrangements in the film. A 213_c peak is chosen as a representative peak since this peak is sensitive to in-plane polarization components along both [100] or [010] directions. For the case of $KNbO_3$ on $GdScO_3$ at 400 K, the 2D RSM of the film peak around the 213_c $GdScO_3$ peak (Figure 3b) shows film-substrate commensuration where additional diffuse scattering patterns near the film peak could not be observed. In the case of low-symmetry phases, we would have expected the formation of ferroelastic twins to generate diffuse scattering around the film position, whereas, in a tetragonal phase that is fully polarized out-of-plane as indicated by SHG measurements, the ferroelastic twin formation is not expected. Thus, X-ray measurements are consistent with the SHG measurements and the phase-field simulations in observing a tetragonal phase at >275 K. When cooled down below the phase transition temperature, the $KNbO_3$ film peaks develop diffuse scattering patterns nearby, which correspond to the formation of twins with an in-plane periodic arrangement. This reflects the symmetry lowering from the high-temperature tetragonal structure to a low-temperature monoclinic phase for the −1.1% biaxially strained thin films, supporting the SHG observations. The tilt of the diffuse satellite peaks can be directly correlated to the tilt of the monoclinic domains themselves relative to the substrate.[33,34] Averaging over several peaks (Figure S17, Supporting Information), this tilt is measured to be 17° ± 4° away from the [110] in-plane direction toward the [001] out-of-plane direction, which agrees with the phase-field microstructure modeling of monoclinic domains at 100 K, which shows a similar tilt of ≈19° away from the [110] direction (Figure 3c, left and bottom panels). Diffraction simulation of the phase-field microstructure at 100 K (Figure 3d) also supports this expectation where diffuse satellites around the 213_c $KNbO_3$ peak show the same tilt of ≈19°, emphasizing the connection between the tilt of the satellite peaks and the tilt of the domains themselves. The same tilt is similarly observed for diffraction simulations around several other peaks as well (Figure S17, Supporting Information) which considerably strengthens our claim. In comparison, diffraction simulation of the phase-field microstructure at 400 K (Figure 3d, right panel) shows diffuse scattering around the 213_c $KNbO_3$ peak without any tilt, consistent with the formations of only tetragonal domain variants with polarization along the [001] or [00$\bar{1}$] directions with 180° domain walls between them. The experimentally measured RSM at 400 K does not show such diffuse scattering patterns around the film peak. This is due to the absence of 180° tetragonal domains in these films. Only the polarization direction pointing upwards from the substrate appears to be stable as confirmed by piezoresponse force microscopy measurements (Section 5 and Figure S23, Supporting Information). Additionally, the experimentally observed diffuse satellite peaks at 100 K correspond to an in-plane domain periodicity of ≈27 nm in agreement with the ≈22 nm periodicity predicted by phase field modeling.

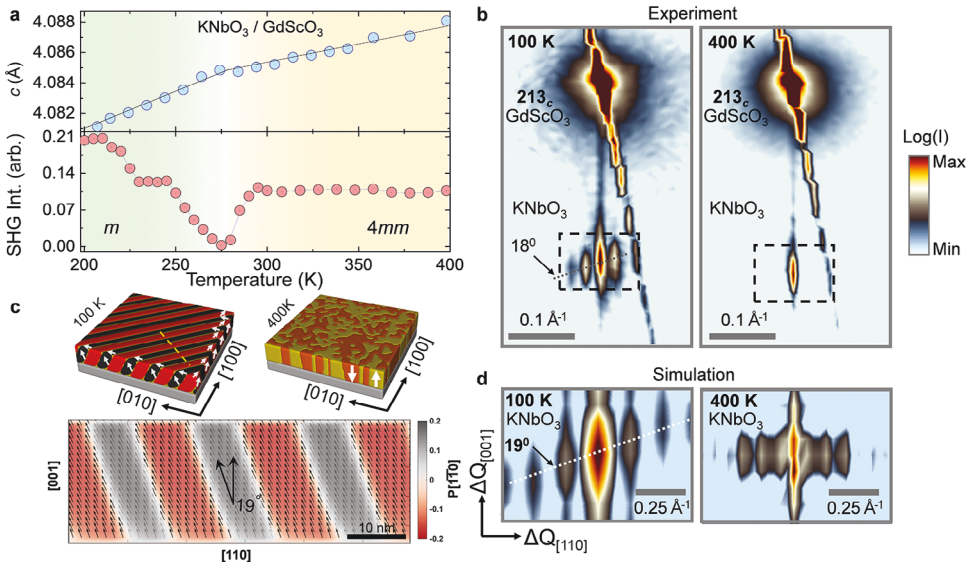

Figure 3. a) (Upper panel) Out-of-plane lattice parameter measured for the $KNbO_3$ film grown on a $GdScO_3$ substrate deduced from the position of the 002_c specular peak between 200 K and 400 K, showing a change of the thermal expansion coefficient at 275 K. The phase transition temperature from the X-ray agrees with the SHG measurements (lower panel, zoomed in from Figure 2c). b) Synchrotron-based x-ray reciprocal space maps (RSM) at 400 K and 100 K for the $KNbO_3$ film grown on a $GdScO_3$ substrate around the 213_c (c stands for cubic) substrate Bragg reflection (tetragonal to monoclinic phase transition found from SHG at 275 K). The strong diagonal streak passing through the substrate peak is an artifact due to the spreading of the signal on the area detector for high intensity and is oriented along the Ewald sphere. Both at 400 K and 100 K, the films are coherent to the substrate but at 100 K, the film peak develops diffuse satellite peaks which are attributed to the formation of periodic monoclinic twin domains. The satellite peaks are tilted away from the in-plane [110] direction toward the [001] direction by 17° ± 4° calculated by averaging over several peaks. The domains exhibit a 27 nm periodicity in the [110] direction extracted from the satellite peak separation. c) (left panel) Phase-field simulated microstructure at 100 K showing monoclinic domains consistent with the domain pattern experimentally observed (left panel of (b)). A vertical cut of this microstructure is shown in the bottom panel along the [110] direction (bottom panel) revealing a tilt of the domain by 19° similar to experimental observations (left panel of (b)). Predicted domain periodicity is measured to be ≈22 nm through phase field simulations matching the experimental observation (≈27 nm). Phase field simulated microstructure at 400 K shows tetragonal domains with no in-plane periodic structures (right panel) consistent with right panel of (b). d) Diffraction simulation of the phase field microstructure at 100 K and 400 K around the 213_c $KNbO_3$ peak (zoomed in to match q-vectors corresponding to dotted boxs in panel (b)) showing a 19° tilt in the diffuse satellites at 100 K matching experimental observations whereas no tilt is seen corresponding to the simulation at 400 K.

5. Ferroelectricity

To test the ferroelectric behavior of $KNbO_3$, thin films were grown on $SrTiO_3$ and $DyScO_3$ substrates with a 15 nm thick $SrRuO_3$ bottom electrode layer. RHEED and RSMs were performed to confirm the crystallinity and commensurate strain nature of the films on the substrate (Figures S18 and S19, Supporting Information). Cross-sectional TEM of $KNbO_3/SrRuO_3/SrTiO_3$ films shows a uniform interface structure without any extended defects suggesting high-quality epitaxial growth (Figure S11, Supporting Information). Temperature-dependent SHG on $KNbO_3$ films with $SrRuO_3$ bottom electrode shows no effect of $SrRuO_3$ on the phase transition temperatures of the $KNbO_3$ films (Figure S20, Supporting Information).

Piezoresponse force microscopy (PFM) and electrical measurements of the switching current were performed on the $Pt/KNbO_3/SrRuO_3/DyScO_3$ capacitors with 21.8 nm thick $KNbO_3$. **Figure** 4a shows a representative PFM switching spectroscopy loop obtained at an arbitrary location on the capacitor at a quasi-static frequency of 0.2 Hz, which exhibits standard ferroelectric d_{33}-V behavior with coercive voltages of −0.5 and 2.2 V. The films appear to be self-poled in the as-grown state with a remanent polarization, P_r, pointing from the bottom to the top of the film. When poled down by applying a bias using the PFM tip, the strong upward built-in field (≈0.8 MV cm^{-1}) causes the downward polarization to relax back to the upward state in seconds (Figures S21–S23, Supporting Information). I–V measurements (Figure 4b) at a frequency of 100 kHz from the capacitors show clear switching current peaks on the negative voltage side, while a high leakage current appears on the positive voltage side obscuring the switching current signal. Additional testing shows that the high leakage on the positive voltage side increases with time. In addition, it can also be seen in Figure 4b that the current for the voltage decreasing from 4 to 0 V is higher than that for the voltage increasing from 0 to 4 V. This leakage, which cannot be subtracted using a standard PUND (positive-up-negative-down) method,[35] prevents measurements of the switching current on the positive bias side. In contrast, the switching current can be measured on the negative bias side using the PUND method (Figure 4c). The extracted switching current peak shows a switching time for the 5 × 5 μm^2 capacitors on the order of 80 ns and a P_r of ≈38 μC cm^{-2}. Nonetheless, further investigation reveals that there is a dynamic leakage current during the polarization switching process that is not subtracted with the standard PUND method (Figure S22, Supporting Information), which suggests that the calculated polarization value is perhaps overestimated.[36,37] Polarization switching in $KNbO_3$

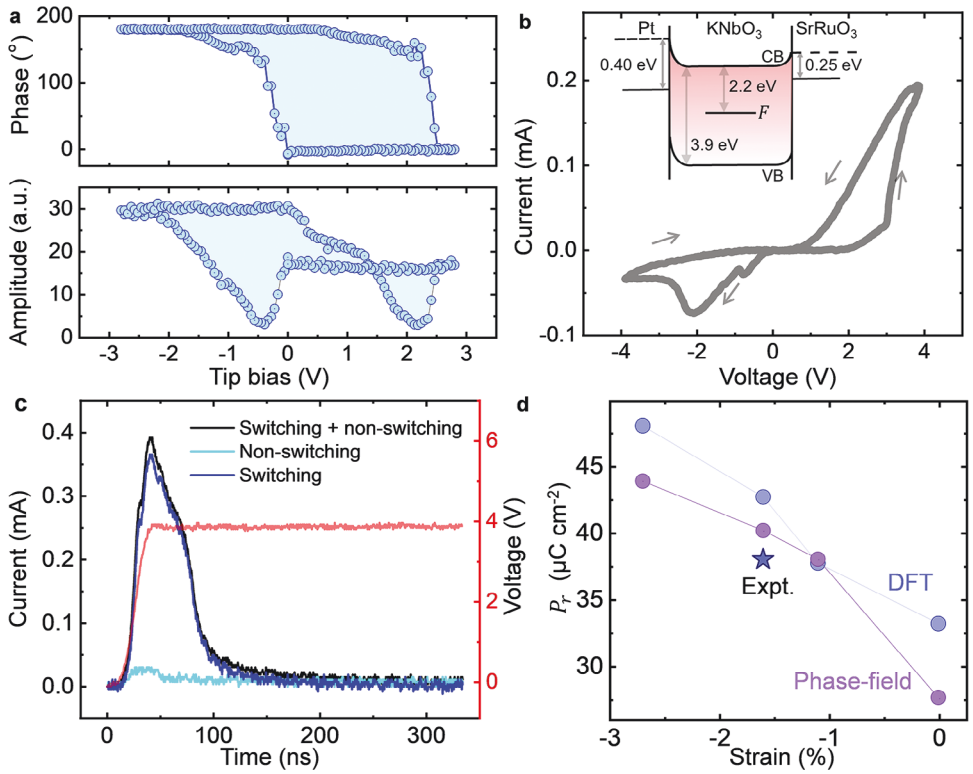

Figure 4. PFM switching spectroscopy and electrical measurements of the switching current on the 5 × 5 μm^2 Pt/$KNbO_3$/$SrRuO_3$/$DyScO_3$ capacitors. a) PFM switching spectroscopy measured at an arbitrary location on the capacitor shows standard ferroelectric d_{33}-V behavior. b) I–V measurement shows switching current peaks on the negative voltage side, while high leakage current smears out the switching peak on the positive side. The inset shows a schematic band diagram of $KNbO_3$ depicting the measured Schottky barrier heights at both Pt-$KNbO_3$ and $SrRuO_3$-$KNbO_3$ interfaces and the known *F*-center (Oxygen-vacancy which traps electrons) energy level in $KNbO_3$.[43,44] c) PUND measurement of the switching peak at −4 V shows a switching time in the order of 80 ns and a remnant polarization of ≈38 μC cm^{-2}. d) Comparison of polarization versus strain predicted from phase-field simulations and DFT calculations along with experimentally observed value from PUND measurements. All values are for the tetragonal phase of $KNbO_3$.

films on $DyScO_3$ and $SrTiO_3$ substrates with $SrRuO_3$ bottom electrode have also been confirmed with PFM measurements (Figure S21, Supporting Information), where the presence of the strong upward built-in fields causes the polarization down state to be very unstable, and the as-grown films are preferentially in the upward single domain states. Figure 4d shows a comparison of the measured P_r with predicted P_r values from phase field simulations and PBEsol calculations, indicating further room for the enhancement of the experimental P_r.

Our current PFM measurements on the Pt/$KNbO_3$/$SrRuO_3$ capacitors show asymmetric leakage currents for opposite polarities. To understand the origin of the leakage current, temperature-dependent IV measurements under DC bias were performed on Pt/$KNbO_3$/$SrRuO_3$/$SrTiO_3$ capacitors. The IV measurements can be fitted to a Schottky emission model (Figures S24 and S25, Supporting Information), suggesting electrode-film interface-controlled Schottky emission to be one of the dominant contributors of leakage in $KNbO_3$ films. The estimated Schottky barrier height is 0.4 ± 0.04 eV for the Pt/$KNbO_3$ interface and 0.25 ± 0.03 eV for the $SrRuO_3$/$KNbO_3$ interface. The asymmetric Schottky barrier height is responsible for the asymmetric leakage current and is due to the different work functions of Pt (5.6 eV[38]) and $SrRuO_3$ (5.2 eV[39]) electrodes and different interface chemistry at each interface (Figure 4b).

To further explore the dielectric response and additional charge transport mechanisms in the $KNbO_3$ film, temperature, and frequency-dependent modulus spectroscopy measurements were performed. The frequency-dependent imaginary part of the electric modulus shows a dielectric relaxation peak with a corresponding Arrhenius activation energy of 0.45 ± 0.04 eV (Figure S27, Supporting Information). We hypothesize that this relaxation process is related to the polaron hopping mechanism which has previously been observed in $KNbO_3$ single crystals.[40,41] Due to high K vapor pressure, K vacancies are common in $KNbO_3$, which subsequently leads to oxygen vacancies. Since these oxygen vacancies are necessary for charge neutrality, they are thermodynamically stable and cannot be removed via an annealing process. Oxygen vacancies can also be formed due to oxygen leaving lattice positions serving as electron donor defects leading to carrier injection in $KNbO_3$.[42] Oxygen vacancies can contribute to both electronic and ionic conductivity in $KNbO_3$ films. Oxygen vacancies in $KNbO_3$ can also serve as electron trapping sites (*F*-center) which produces deep energy levels, ≈2.2 eV below the conduction band.[43,44] Finally, migration of K^+ ions and oxygen vacancies (activation energies of 0.6 and 1.2 eV respectively)[45] and the formation of conductive domain walls and pinholes across a thin film can also contribute to leakage in $KNbO_3$ thin films.

Our present investigations in strain-tuned $KNbO_3$ films present a unique opportunity in $KNbO_3$ where strain can not only be employed to enhance ferroelectric properties in $KNbO_3$ but also these properties can be accessed stably across a wide temperature range of operation by pushing out phase transitions which would otherwise lead to divergence of ferroelectric properties. Though further work is necessary to understand the nature and role of intrinsic defects in $KNbO_3$ thin films, SHG experiments show the robustness of $KNbO_3$ films at high temperatures ranging up to ≈975 K. Notably, surface capping of $KNbO_3$, the development of $KNbO_3$-based superlattice heterostructures, and slightly doping the film with electron acceptors would not only further enhance the stability of $KNbO_3$ from the formation of intrinsic K and O vacancy point defects, but also would allow the growth of thicker coherently strained films avoiding mechanical sources of leakage like pinhole formations.

6. Conclusion

In summary, our experiments and simulations demonstrate that biaxially strained $KNbO_3$ films result in the stabilization of a single tetragonal phase throughout the entire temperature range from 10 K to 975 K in contrast to four competing phases observed in bulk single crystals; this is challenging to achieve in other competing Pb-free ferroelectrics such as $BaTiO_3$ and $Na_xK_{1-x}NbO_3$. Concomitantly, a large enhancement in the tetragonality through strain is observed with its c/a ratio reaching values that exceed even those of bulk $PbTiO_3$. A ≈200% increase in the tetragonal phase optical second harmonic generation coefficients over bulk single crystal values is observed. A dramatic T_c enhancement well beyond its decomposition and melting temperatures are seen with a 3 × higher tunability, $\frac{dT_c}{d\epsilon}$, as compared to all other strain-tuned perovskite oxides. A broad design trend gleaned from this study is that for tetragonal perovskite ferroelectrics, a high T_c is achieved by maximizing electrostriction and minimizing elastic compliance (Figure S3, Supporting information). Importantly, there are optimal values of electrostriction and compliance that maximize P_r. For $KNbO_3$, its superior electrostriction and low elastic stiffness coefficients compared to similar materials result in a large and highly strain-tunable T_c in addition to a competitive magnitude and tunability in P_r. All these observations render strained $KNbO_3$ thin films as a strong, thermally stable lead-free ferroelectric with a large operating temperature regime suitable for a wide range of applications.

7. Experimental Section

Thin Film Synthesis and Characterization: Epitaxial thin films of $KNbO_3$ were grown using a Vecco Gen 10 MBE system. A molecular beam of NbO_2 (gas) flux was generated from an effusion cell containing Nb_2O_5 (H.C. Stark 99.99%) contained in an iridium crucible. NbO_2 is the most volatile species in the growth temperature range.[46] Potassium was evaporated from an effusion cell containing an indium-rich (≈4:1 In:K ratio) mixture of potassium and indium so it forms the air-stable intermetallic In4K.[47] The K-In alloy was prepared in a glove box and contained in a titanium crucible. Once prepared, it can be exposed to air, facilitating its handling and loading. The vapor pressure of potassium was more than 10^{10} times higher than indium at the K-In cell temperature of 300 - 400 °C.[48] $GdScO_3$ $(110)_o$, and $DyScO_3$ $(110)_o$ (Crystec GmbH) substrates were used as received and the $SrTiO_3$ (001) substrates were terminated following the procedure developed by Koster.[49]

Films were grown by co-deposition of potassium, niobium, and ozone at a substrate temperature of 700–650 °C as measured by an optical pyrometer operating at a wavelength of 1550 nm. The pyrometer measures the temperature of the platinum coating that had been evaporated on the backside of the substrate to facilitate radiative heat transfer from the SiC heating element of the MBE system to the substrate. The K:Nb flux ratio was kept at ≈10:1. A mixture of ozone and oxygen (10% O_3 + 90% O_2) was used as the oxidant. The films were grown at an oxidant background pressure of 1×10^{-6} Torr. Typical fluxes for the sources were $(1 - 2) \times 10^{13}$ atoms cm^{-2} s^{-1} for NbO_2 and $(1 - 4) \times 10^{14}$ atoms cm^{-2} s^{-1} for potassium, determined by a quartz crystal microbalance (QCM), with an accuracy of ≈15%. In a typical growth experiment, the potassium flux was measured first, followed by NbO_2 to ensure that the QCM was as close to room temperature as possible for the most accurate reading. For a more detailed description, the reader was referred to an identical procedure reported for $KTaO_3$.[50] Co-deposition with these fluxes results in a $KNbO_3$ film growth rate of ≈0.3 Å s^{-1}.

X-ray diffraction (XRD), X-ray reflectometry (XRR), and RSM measurements were carried out using a PANalytical Empyrean diffractometer with Cu $K\alpha_1$ radiation. The raw XRR spectra were analyzed using the PANalytical X´Pert Reflectivity software package and the layer thickness was derived from a fast Fourier transform (FFT) after manually defining the critical angle to account for refractive effects. In situ reflection high-energy electron diffraction (RHEED) patterns were recorded using KSA-400 software and a Staib electron source operated at 14 kV and a filament current of 1.5 A. The morphology of the film surface was characterized using an Asylum Cypher ES environmental AFM.

Transmission Electron Microscopy: The cross-sectional samples for scanning transmission electron microscopy (STEM) were prepared using a standard focused ion beam lift-out process. The $KNbO_3$ thin film on the $SrTiO_3$ substrate was milled using the FEI Helios NanoLab 600 DualBeam, while the samples on $GdScO_3$ and $DyScO_3$ substrates were milled using the Helios G4 UX DualBeam system. All samples were initially thinned with 5 kV Ga ions and then polished at 2 kV to minimize surface damage. HAADF-STEM images of $KNbO_3$ samples on $GdScO_3$ and $DyScO_3$ were obtained using the Spectra 300 X-CFEG microscope with a 60–200 mrad HAADF detector. For the $KNbO_3$ film on $SrTiO_3$, the Thermo Scientific Themis Z S/TEM with a 64–200 mrad HAADF detector was used. Both microscopes operated at 200 kV with a semi-convergence angle of 30 mrad. To improve the signal-to-noise ratio, HAADF-STEM images were captured as a series of 20 fast scan images (2048 × 2048 pixels, 200 ns per frame) and then averaged them. STEM energy-dispersive X-ray (EDX) spectroscopy data for films on $GdScO_3$ and $DyScO_3$ were collected using a steradian Dual-X EDX detector. The resulting spectrum was then denoised using principal component analysis.

Second Harmonic Generation (SHG) Measurement: SHG polarimetry and temperature-dependent measurements were done with femtosecond pulses at $\lambda = 800$ nm fundamental light from a regeneratively amplified Spectra-Physics Solstice Ace Ti:Sapphire laser system (1kHz, 100 fs). The schematic of the setup is shown in Figure 2a. Linearly polarized light incident on the sample at an incidence angle θ generate second harmonic light at $\lambda = 400$ nm. The *p*-polarized and *s*-polarized SHG intensities were spectrally filtered and measured by a photomultiplier tube through lock-in amplifier (SR830) detection. Polar plots were generated by rotating the polarization angle (φ) of the incident fundamental light by a half-wave plate. Temperature-dependent measurements were done through a Janis 300 gas flow cryostat for low-temperature and a home-built heating stage for high-temperature experiments.

Synchrotron-Based Reciprocal Space Mapping: Synchrotron x-ray diffraction experiments were performed on the ID4B (QM2) beamline at the Cornell high energy synchrotron source (CHESS). The incident X-ray energy was 50 keV (λ = 0.247 Å), which was selected using a double-bounce diamond monochromator. An area detector array (Pilatus 6M) was used to collect the scattering intensities in a reflection geometry. The sample was rotated with a 1° tilt through 180° rotations, sliced into 0.1° frames. Geometric parameters of the Pilatus 6M detector such

as detector distance, tilting, rotation, and direct beam position were extracted using standard CeO_2 powder. The uncertainty in temperature was <10 K.

X-Ray Photoelectron Spectroscopy: The XPS experiment was performed using the Physical Electronics VersaProbe III instrument with a monochromatic Al $K\alpha$ x-ray source ($h\nu$ = 1486.6 eV) and a concentric hemispherical analyzer. Charge neutralization was performed using low-energy electrons (<5 eV) and argon ions. The binding energy axis was calibrated using sputter-cleaned Cu (Cu $2p_{3/2}$ = 932.62 eV, Cu $3p_{3/2}$ = 75.1 eV) and Au foils (Au $4f_{7/2}$ = 83.96 eV). Measurements were made at a takeoff angle of 45° with respect to the sample surface plane. This resulted in a typical sampling depth of 3–6 nm. On homogeneous samples, major elements (>5 atom%) tend to have standard deviations of <3%, while minor elements can be significantly higher. The analysis size was 200 µm in diameter.

PFM Spectroscopy Measurements: The PFM switching spectroscopy data were measured using an atomic force microscopy system (MFP3D, Asylum Research) with Pt-coated tips (PPP-EFM, Nanosensors) in the resonance enhanced mode (DART) with AC-modulation voltage of 0.2 V at 340 kHz. DC voltage was applied to the top electrodes in the pulsed mode, where the pulse-on period is for polarization switching and the pulse-off period is for PFM signal detection.

Pt Top Electrodes Deposition: The Pt top electrodes with a thickness of ≈15 nm were deposited ex situ by pulsed laser deposition (PLD) in vacuum at room temperature. 5 × 5 µm^2 electrode patterns were prepared using a standard liftoff approach with a laser lithography system (Heidelberg DWL 66FS).

PUND and I–V Measurements: A function generator (Keysight 33621A) was used for voltage pulse generation, and an oscilloscope (Tektronix TDS 3014B) was used for recording the switching current signal. Standard triangular waves at 100 kHz were used for the *I–V* measurements, and square pulses of 500 ns in width with one negative pulse followed by two positive and then two negative pulses were used for the PUND measurements (see Figure S17, Supporting Information). The pulse rise time is ≈20 ns. All voltages were applied to the top electrodes through the PFM tip.

Leakage Current and Modulus Spectroscopy Measurements: To investigate the dominant conduction mechanisms responsible for the rise in leakage current in $KNbO_3$ films, leakage current measurements were performed on 21.8 nm thick $KNbO_3$ films grown on $DyScO_3$ with a 15 nm thick $SrRuO_3$ bottom electrode, using a 4140 Pico-Ampere Meter/DC Voltage Source (Hewlett Packard). 100 nm thick Pt electrodes which were lithographically patterned into 50 µm × 50 µm squares, were used as the top electrode.

To further explore additional charge transport mechanisms in the $KNbO_3$ film, temperature-dependent modulus spectroscopy measurements were performed using a Solartron 1260 Impedance analyzer with a l00 mV AC amplitude, over a frequency range from 1 MHz to 0.01 Hz.

Phase-Field Modeling: Using the phase field method, the evolution of the ferroelectric polarization (P_i) was governed by the time-dependent Ginzburg Landau equation:

$$\gamma_{ij}\frac{\partial P_j(x_i,\ t)}{\partial t} = \frac{\delta F}{\delta P_i(x_i, t)} \tag{2}$$

where γ_{ij} is the kinetic coefficient tensor which is chosen to be isotropic and F is the total free energy of the system which is the integral of all energy density components:

$$F = \iiint_V \left[f_{landau}(P_i) + f_{grad}(\nabla P_i) + f_{elas}\left(P_i, \varepsilon_{ij}\right) + f_{elec}(P_i, E_i)\right] dV \tag{3}$$

where f_{landau}, f_{grad}, f_{elas} and f_{elec} denote the Landau free-energy density, the gradient energy density, the elastic energy density, and the electrostatic energy density respectively, and V is the volume of the system.

The Landau free energy density describes the intrinsic stability of the ferroelectric phases compared to the high symmetry phase ($m\bar{3}m$) as a Taylor expansion of the polarization about the high symmetry phase:

$$\begin{aligned} f_{landau}(P_i) = {} & \alpha_1(T)\left(P_1^2+P_2^2+P_3^2\right)+\alpha_{11}\left(P_1^4+P_2^4+P_3^4\right) \\ & +\alpha_{12}\left(P_1^2P_2^2+P_1^2P_3^2+P_2^2P_3^2\right)+\alpha_{111}\left(P_1^6+P_2^6+P_3^6\right) \\ & +\alpha_{112}\left(P_1^4\left(P_2^2+P_3^2\right)+P_2^4\left(P_1^2+P_3^2\right)+P_3^4\left(P_1^2+P_2^2\right)\right) \\ & +\alpha_{123}P_1^2P_2^2P_3^2+\alpha_{1111}\left(P_1^8+P_2^8+P_3^8\right)+\alpha_{1112}\left(P_1^6\left(P_2^2+P_3^2\right)\right. \\ & \left.+P_2^6\left(P_1^2+P_3^2\right)+P_3^6\left(P_1^2+P_2^2\right)\right) \\ & +\alpha_{1122}\left(P_1^4P_2^4+P_2^4P_3^4+P_3^4P_1^4\right) \\ & +\alpha_{1123}\left(P_1^4P_2^2P_3^2+P_1^2P_2^4P_3^2+P_1^2P_2^2P_3^4\right) \end{aligned} \tag{4}$$

The Landau expansion coefficients were adjusted from the work of Liang[11] to fit with experimentally measured polarization and dielectric properties.[51–53] The revised set of coefficients is listed under Table S1 in Section S1 (Supporting Information).

The gradient energy density is represented by:

$$f_{grad} = \frac{1}{2}G_{ijkl}\frac{\partial P_i}{\partial x_j}\frac{\partial P_k}{\partial x_l} \tag{5}$$

where G_{ijkl} is the gradient energy tensor where the non-zero coefficients are chosen to be G_{11} = 0.6, G_{22} = −0.6 and G_{44} = 0.6 and the units are normalized by $\alpha_1 l_o^2$ where α_1 is the first Landau expansion coefficient and l_o is chosen as 1 nm per grid.

The elastic energy density is calculated as:

$$f_{elas}\left(P_i,\ \varepsilon_{ij}\right) = \frac{1}{2}c_{ijkl}\left(\varepsilon_{ij}-\varepsilon_{ij}^o\right)\left(\varepsilon_{kl}-\varepsilon_{kl}^o\right) \tag{6}$$

where c_{ijkl} represents the stiffness tensor, ε_{ij} is the total strain using the parent cubic phase as a reference, and ε_{ij}^o is the eigenstrain which is dictated by the ferroelectric polarization and the electrostrictive tensor Q_{ijkl} as:

$$\varepsilon_{ij}^o = Q_{ijkl}P_kP_l \tag{7}$$

The elastic constant tensor components and electrostrictive coefficients used in this work are listed in Table S2 in Section S1 (Supporting Information).

The electrostatic energy density can be expressed as:

$$f_{elec}(P_i,\ E_i) = -E_iP_i - \frac{1}{2}\varepsilon_o\kappa_{ij}E_iE_j \tag{8}$$

where E_i is the component of the electric field, ε_o is the dielectric permittivity of vacuum and κ_{ij} is the background dielectric susceptibility which accounts for the contributions to the total dielectric susceptibility beyond the ferroelectric soft mode following the work of Tagentsev.[54]

The evaluation of the elastic and electrostatic energy contributions in the phase-field method could be found in the existing literature.[55–57] At each time step, the electrical and mechanical equilibrium equations were solved under short-circuit and thin-film boundary conditions respectively.

For the simulations, a spatially discretized system of 128Δx × 128Δy × 36Δz grids was employed with a grid spacing $\Delta x = \Delta y = \Delta z$ = 1 nm. The film thickness was set to 20Δx, and the substrate was 10Δx, with a 4Δx layer of air above the film. The in-plane strains ε_{11} and ε_{22} were set equal to the misfit strains imposed by the lattice mismatch with the substrate. An initial random polarization distribution with a small magnitude of fluctuations of ΔP = 0.1 Cm^{-2} was started and let the system evolve to equilibrium.

The details on the construction of the phase diagram are provided in Note S1 (Supporting Information).

Diffraction Simulation: The diffraction intensity (I) was calculated at the reciprocal space position $\boldsymbol{q}$ from:

$$I\ (\boldsymbol{q}) = |F\ (\boldsymbol{q})|^2 \tag{9}$$

where F is the structure factor obtained by:

$$F\ (\boldsymbol{q}) = \sum_{m,n} f_n e^{-\boldsymbol{q}\cdot\boldsymbol{r}_{m,n}} \tag{10}$$

where m is the unit cell index, n is the index of the atoms within the unit cell, and f_n is the atomic form factor of the n-th atom which is comprised of a real and imaginary part:

$$f_n = f_n^1 + if_n^2 \tag{11}$$

The atomic form factors for the constituent atoms were obtained from the tabulated atomic data,[58] assuming a photon energy of 10 KeV. The position of each atom ($\boldsymbol{r}_{m,n}$) was calculated assuming a linear dependence of the atomic positions upon the polar order, i.e.,:

$$\boldsymbol{r}_{m,n} = \boldsymbol{R}_{m,n} + s_n \boldsymbol{P}_m \tag{12}$$

where $\boldsymbol{R}_{m,n}$ is the reference position in the absence of a polarization and $\boldsymbol{s}_n$ are atomic site-specific displacement coefficients relating the polarization to the atomic displacement. Atomic form factors and site-specific displacement coefficients are given in Table S4 (Supporting Information).

Density Functional Theory: The different phases were structurally optimized in the framework of density-functional theory (DFT) with the open-source software ABINIT.[59–61] A plane-wave basis set with a kinetic energy cutoff of 49 Ha was used to expand the wavefunctions. Optimized norm-conserving Vanderbilt pseudopotentials from the PseudoDojo[62,63] (v0.4.1) were adopted and the exchange-correlation energy was modeled using the Perdew–Burke–Ernzerhof generalized-gradient approximation modified for solids (GGA-PBEsol).[64,65] The Brillouin zone was sampled with a Monkhorst–Pack[66,67] 8 × 8 × 8 k-point mesh and the self-consistent field cycles were converged until the residual on the potential reached 10^{-12}. The structures were relaxed until a maximum force of 2.5 meV Å^{-1} on each atom was reached. The local-density approximation[68] and the GGA-PBE exchange correlation were also tested, but the PBEsol functional resulted in the best c/a ratio for the tetragonal and orthorhombic phases. For each phase, the in-plane lattice parameters were fixed while the out-of-plane lattice parameter and the internal atomic positions were allowed to relax. For the monoclinic phase, since it presents too many degrees of freedom to adopt the same methodology, the in-plane lattice parameters were set to the average values obtained by the phase-field simulations at 25K for the two strains corresponding to the $GdScO_3$ and $DyScO_3$ substrates.

The polarization was computed with the Vienna ab initio simulation package (VASP v6.3.0).[69–72] The exchange-correlation energy was modeled with the GGA-PBE and the projector augmented wave method (PAW) method was used.[73] The wavefunctions were expanded on a plane-wave basis set with a kinetic energy cutoff of 680 eV. A 6 × 6 × 6 Γ-centered k-point mesh was adopted to sample the Brillouin zone, and the total energy was converged to 1 μeV in the electronic self-consistent loops. The polarization calculations were automated with the atomate2 python package.[74]

Supporting Information

Supporting Information is available from the Wiley Online Library or from the author.

Acknowledgements

S.H. and T.S. contributed equally to this work. S.H., A.M., J.W.F., A.M.L., V.A.S., and V.G. acknowledge support from the DOE-BES grant DE-SC0012375 for thin film growth efforts (S.H.), optical SHG experiments (S.H., V.G.), x-ray characterization (S.H., A.M., J.W.F., V.A.S., V.G.), and manuscript preparation. This work made use of the synthesis and electron microscopy facilities of the Platform for the Accelerated Realization, Analysis, and Discovery of Interface Materials (PARADIM), which are supported by the National Science Foundation under Cooperative Agreement No. DMR-2039380. TS, MRB, DAM, and DGS, also acknowledge the support of the National Science Foundation under Cooperative Agreement No. DMR-2039380. A.R., U.S., T.K., R.E.H., L.Q.C., and V.G. acknowledge support from the U.S. Department of Energy, Office of Science, Office of Basic Energy Sciences, under Contract No. DE-SC0020145 for the phase-field simulations (A.R., U.S., L.Q.C.) and part of the growth efforts (T.K., R.E.H, and V.G.). A.R. also acknowledges the support of the National Science Foundation Graduate Research Fellowship Program under Grant No. DGE1255832. The phase-field simulations in this work were performed using Bridges-2 at the Pittsburg Supercomputing Center through allocation MAT230041 from the ACCESS program, which is supported by National Science Foundation grants #2138259, #2138286, #2138307, #2137603 and #2138296.The PFM studies at UNL have been supported by the UNL Grand Challenges catalyst award "Quantum Approaches addressing Global Threats". B.Z.G. and A.S. acknowledge support for the generation of 3D reciprocal space maps from the U.S. Department of Energy, Office of Science, Office of Basic Energy Sciences, under Contract No. DE-SC0019414. V.T. acknowledges the support from the FRS-FNRS through an FRIA Grant. Computational resources have been provided by the supercomputing facilities of the Université Catholique de Louvain (CISM/UCL) and the Consortium des Équipements de Calcul Intensif en Fédération Wallonie Bruxelles (CÉCI) funded by the Fond de la Recherche Scientifique de Belgique (F.R.S.-FNRS) under convention 2.5020.11 and by the Walloon Region. The present research benefited from computational resources made available on Lucia, the Tier-1 supercomputer of the Walloon Region, infrastructure funded by the Walloon Region under grant agreement No. 1910247. Research conducted at the Center for High-Energy X-ray Science (CHEXS) was supported by the National Science Foundation (BIO, ENG, and MPS Directorates) under award DMR-1829070. X.L and X.X. acknowledge the support of Intel. This work made use of a Helios FIB supported by NSF (grant no. DMR-1539918) and the Cornell Center for Materials Research (CCMR) Shared Facilities, which were supported through the NSF MRSEC Program (grant no. DMR-1719875). The Thermo Fisher Spectra 300 X-CFEG was acquired with support from PARADIM (NSF MIP DMR-2039380) and Cornell University. Part of the Electron microscopy experiment was performed at the Center for Electron Microscopy and Analysis (CEMAS) at The Ohio State University. S.S. and V.G. acknowledge support from National Science Foundation grant number NSF DMR-2210933 for optical SHG characterization. For electrical leakage measurements, the authors acknowledge the Center for 3D Ferroelectric Microelectronics (3DFeM), an Energy Frontier Research Center funded by the U.S. Department of Energy (DOE), Office of Science, Basic Energy Sciences, under Award No. DE-SC0021118. [Correction added on November 19, 2024, after first online publication: Data Availability Section has been updated.]

Conflict of Interest

The authors declare no conflict of interest.

Data Availability Statement

The data that support the findings of this study are available within the article. Additional data related to the film growth and structural characterization by XRD and STEM are available at https://doi.org/10.34863/fs5e-s772. Any additional data connected to the study are available from the corresponding author upon reasonable request.

Keywords

ferroelectrics, phase-field modeling, second harmonic generation, strain-tuning, thin films

Received: June 18, 2024
Revised: October 24, 2024
Published online: November 12, 2024

[1] D. G. Schlom, L.-Q. Chen, C.-B. Eom, K. M. Rabe, S. K. Streiffer, J.-M. Triscone, *Annu. Rev. Mater. Res.* **2007**, *37*, 589.
[2] K. J. Choi, M. Biegalski, Y. L. Li, A. Sharan, J. Schubert, R. Uecker, P. Reiche, Y. B. Chen, X. Q. Pan, V. Gopalan, L.-Q. Chen, D. G. Schlom, C. B. Eom, *Science* **2004**, *306*, 1005.
[3] R. Xu, J. Huang, E. S. Barnard, S. S. Hong, P. Singh, E. K. Wong, T. Jansen, V. Harbola, J. Xiao, B. Y. Wang, S. Crossley, D. Lu, S. Liu, H. Y. Hwang, *Nat. Commun.* **2020**, *11*, 3141.
[4] J. H. Haeni, P. Irvin, W. Chang, R. Uecker, P. Reiche, Y. L. Li, S. Choudhury, W. Tian, M. E. Hawley, B. Craigo, A. K. Tagantsev, X. Q. Pan, S. K. Streiffer, L. Q. Chen, S. W. Kirchoefer, J. Levy, D. G. Schlom, *Nature* **2004**, *430*, 758.
[5] J. H. Lee, L. Fang, E. Vlahos, X. Ke, Y. W. Jung, L. F. Kourkoutis, J.-W. Kim, P. J. Ryan, T. Heeg, M. Roeckerath, V. Goian, M. Bernhagen, R. Uecker, P. C. Hammel, K. M. Rabe, S. Kamba, J. Schubert, J. W. Freeland, D. A. Muller, C. J. Fennie, P. Schiffer, V. Gopalan, E. Johnston-Halperin, D. G. Schlom, *Nature* **2010**, *466*, 954.
[6] J. Wang, J. B. Neaton, H. Zheng, V. Nagarajan, S. B. Ogale, B. Liu, D. Viehland, V. Vaithyanathan, D. G. Schlom, U. V. Waghmare, N. A. Spaldin, K. M. Rabe, M. Wuttig, R. Ramesh, *Science* **2003**, *299*, 1719.
[7] R. J. Zeches, M. D. Rossell, J. X. Zhang, A. J. Hatt, Q. He, C.-H. Yang, A. Kumar, C. H. Wang, A. Melville, C. Adamo, G. Sheng, Y.-H. Chu, J. F. Ihlefeld, R. Erni, C. Ederer, V. Gopalan, L. Q. Chen, D. G. Schlom, N. A. Spaldin, L. W. Martin, R. Ramesh, *Science* **2009**, *326*, 977.
[8] F. Eltes, G. E. Villarreal-Garcia, D. Caimi, H. Siegwart, A. A. Gentile, A. Hart, P. Stark, G. D. Marshall, M. G. Thompson, J. Barreto, J. Fompeyrine, S. Abel, *Nat. Mater.* **2020**, *19*, 1164.
[9] V. S. Puli, A. Jayakrishnan, D. K. Pradhan, K. Madgula, S. N. Babu, D. B. Chrisey, R. S. Katiyar, A. Reed, M. McConney, T. Back, R. M. Van Ginhoven, S. Heidger, *Energy Storage* **2023**, *5*, e359.
[10] H. Zhang, T. Wei, Q. Zhang, W. Ma, P. Fan, D. Salamon, S.-T. Zhang, B. Nan, H. Tan, Z.-G. Ye, *J. Mater. Chem. C Mater.* **2020**, *8*, 16648.
[11] L. Liang, Y. L. Li, L.-Q. Chen, S. Y. Hu, G.-H. Lu, *J. Appl. Phys.* **2009**, *106*, 104118.
[12] K. Yamanouchi, H. Odagawa, T. Kojima, T. Matsumura, *Electron. Lett.* **1997**, *33*, 193.
[13] K. Nakamura, T. Tokiwa, Y. Kawamura, *J. Appl. Phys.* **2002**, *91*, 9272.
[14] T. T. A. Lummen, J. Leung, A. Kumar, X. Wu, Y. Ren, B. K. VanLeeuwen, R. C. Haislmaier, M. Holt, K. Lai, S. V. Kalinin, V. Gopalan, *Adv. Mater.* **2017**, *29*, 1700530.
[15] L. Bogula, L. von Helden, C. Richter, M. Hanke, J. Schwarzkopf, M. Schmidbauer, *Nano Futures* **2020**, *4*, 035005.
[16] L. von Helden, L. Bogula, P.-E. Janolin, M. Hanke, T. Breuer, M. Schmidbauer, S. Ganschow, J. Schwarzkopf, *Appl. Phys. Lett.* **2019**, *114*, 232905.
[17] M. Schmidbauer, D. Braun, T. Markurt, M. Hanke, J. Schwarzkopf, *Nanotechnology* **2017**, *28*, 24LT02.
[18] M. Adachi, Y. Akishige, T. Asahi, K. Deguchi, K. Gesi, K. Hasebe, T. Hikita, T. Ikeda, Y. Iwata, M. Komukae, T. Mitsui, E. Nakamura, N. Nakatani, M. Okuyama, T. Osaka, A. Sakai, E. Sawaguchi, Y. Shiozaki, T. Takenaka, K. Toyoda, T. Tsukamoto, T. Yagi, in *Oxides*, Springer Nature, Berlin, Germany **2001**, pp. 1–20.
[19] V. Gopalan, R. Raj, *Appl. Phys. Lett.* **1996**, *68*, 1323.
[20] V. Gopalan, R. Raj, *J. Am. Ceram. Soc.* **1995**, *78*, 1825.
[21] V. Gopalan, R. Raj, *J. Appl. Phys.* **1997**, *81*, 865.
[22] Y. Luo, Z. Wang, Y. Chen, M. Qin, Z. Fan, M. Zeng, G. Zhou, X. Lu, X. Gao, D. Chen, J.-M. Liu, *ACS Appl. Mater. Interfaces* **2023**, *15*, 16902.
[23] M. V. Romanov, I. E. Korsakov, A. R. Kaul, S. Y. Stefanovich, I. A. Bolshakov, G. Wahl, *Chem. Vap. Deposition* **2004**, *10*, 318.
[24] T. Saito, T. Wada, H. Adachi, I. Kanno, *Jpn. J. Appl. Phys.* **2004**, *43*, 6627.
[25] T.-H. Lee, H.-G. Hwang, J.-U. Woo, D.-H. Kim, T.-W. Kim, S. Nahm, *ACS Appl. Mater. Interfaces* **2018**, *10*, 25673.
[26] T.-H. Lee, D.-H. Kim, B.-Y. Kim, H.-Y. Choi, J.-H. Oh, C.-Y. Kang, S. Nahm, *Acta Mater.* **2016**, *112*, 53.
[27] C. Ederer, N. A. Spaldin, *Phys. Rev. Lett.* **2005**, *95*, 257601.
[28] N. A. Pertsev, V. G. Kukhar, H. Kohlstedt, R. Waser, *Phys. Rev. B* **2003**, *67*, 054107.
[29] S. A. Denev, T. T. A. Lummen, E. Barnes, A. Kumar, V. Gopalan, *J. Am. Ceram. Soc.* **2011**, *94*, 2699.
[30] R. Zu, B. Wang, J. He, J.-J. Wang, L. Weber, L.-Q. Chen, V. Gopalan, *npj Comput. Mater.* **2022**, *8*, 246.
[31] R. Zu, B. Wang, J. He, L. Weber, A. Saha, L.-Q. Chen, V. Gopalan, *npj Comput. Mater.* **2024**, *10*, 64.
[32] S. Singh, J. P. Remeika, J. R. Potopowicz, *Appl. Phys. Lett.* **1972**, *20*, 135.
[33] A. S. Everhardt, S. Matzen, N. Domingo, G. Catalan, B. Noheda, *Adv. Electron. Mater.* **2016**, *2*, 1500214.
[34] Z. Shao, N. Schnitzer, J. Ruf, O. Y. Gorobtsov, C. Dai, B. H. Goodge, T. Yang, H. Nair, V. A. Stoica, J. W. Freeland, J. P. Ruff, L.-Q. Chen, D. G. Schlom, K. M. Shen, L. F. Kourkoutis, A. Singer, *Proceedings of the National Academy of Sciences* **2023**, *120*, e2303312120.
[35] J. F. Scott, L. Kammerdiner, M. Parris, S. Traynor, V. Ottenbacher, A. Shawabkeh, W. F. Oliver, *J. Appl. Phys.* **1988**, *64*, 787.
[36] G. Schönweger, N. Wolff, M. R. Islam, M. Gremmel, A. Petraru, L. Kienle, H. Kohlstedt, S. Fichtner, *Adv. Sci.* **2023**, *10*, 202302296.
[37] H. Lu, G. Schönweger, A. Petraru, H. Kohlstedt, S. Fichtner, A. Gruverman, *Adv. Funct. Mater.* **2024**, *34*, 2315169.
[38] B. Ofuonye, J. Lee, M. Yan, C. Sun, J.-M. Zuo, I. Adesida, *Semicond. Sci. Technol.* **2014**, *29*, 095005.
[39] V. S. Kumar, M. K. Niranjan, *J. Appl. Phys.* **2014**, *115*, 173705.
[40] S. Torbrügge, M. Imlau, B. Schoke, C. Merschjann, O. F. Schirmer, S. Vernay, A. Gross, V. Wesemann, D. Rytz, *Phys. Rev. B* **2008**, *78*, 125112.
[41] J. Handerek, R. Manka, A. Aleksandrowicz, J. Szatanek, *Ferroelectrics* **1978**, *22*, 735.
[42] N. Zhong, S. Okamura, K. Uchiyama, T. Shiosaki, *Appl. Phys. Lett.* **2005**, *87*, 252901.
[43] R. I. Eglitis, E. A. Kotomin, A. V. Postnikov, N. E. Christensen, M. A. Korotin, G. Borstel, *Ferroelectrics* **1999**, *229*, 69.
[44] R. I. Eglitis, N. E. Christensen, E. A. Kotomin, A. V. Postnikov, G. Borstel, *Phys. Rev. B* **1997**, *56*, 8599.
[45] R. I. Eglitis, E. A. Kotomin, G. Borstel, *physica status solidi c* **2005**, *2*, 113.
[46] K. M. Adkison, S.-L. Shang, B. J. Bocklund, D. Klimm, D. G. Schlom, Z.-K. Liu, *APL Mater* **2020**, *8*, 081110.
[47] H. Okamoto, *J. Phase Equilib.* **1992**, *13*, 217.
[48] R. E. Honig, D. A. Kramer, *RCA Review* **1969**, *30*, 567.
[49] G. Koster, B. L. Kropman, G. J. H. M. Rijnders, D. H. A. Blank, H. Rogalla, *Mater. Sci. Eng., B* **1998**, *56*, 209.
[50] T. Schwaigert, S. Salmani-Rezaie, M. R. Barone, H. Paik, E. Ray, M. D. Williams, D. A. Muller, D. G. Schlom, K. Ahadi, *J. Vac. Sci. Technol. A* **2023**, *41*, 022703.
[51] A. Nazeri-Eshghi, A. X. Kuang, J. D. Mackenzie, *J. Mater. Sci.* **1990**, *25*, 3333.
[52] S. Triebwasser, *Phys. Rev.* **1956**, *101*, 993.
[53] G. Shirane, H. Danner, A. Pavlovic, R. Pepinsky, *Phys. Rev.* **1954**, *93*, 672.
[54] A. K. Tagantsev, *Ferroelectrics* **1986**, *69*, 321.
[55] L. Q. Chen, *J. Am. Ceram. Soc.* **2008**, *91*, 1835.
[56] Y. L. Li, S. Y. Hu, Z. K. Liu, L. Q. Chen, *Acta Mater.* **2002**, *50*, 395.
[57] Y. L. Li, S. Y. Hu, Z. K. Liu, L. Q. Chen, *Appl. Phys. Lett.* **2002**, *81*, 427.
[58] B. L. Henke, E. M. Gullikson, J. C. Davis, *At. Data Nucl. Data Tables* **1993**, *54*, 181.

[59] A. H. Romero, D. C. Allan, B. Amadon, G. Antonius, T. Applencourt, L. Baguet, J. Bieder, F. Bottin, J. Bouchet, E. Bousquet, F. Bruneval, G. Brunin, D. Caliste, M. Côté, J. Denier, C. Dreyer, P. Ghosez, M. Giantomassi, Y. Gillet, O. Gingras, D. R. Hamann, G. Hautier, F. Jollet, G. Jomard, A. Martin, H. P. C. Miranda, F. Naccarato, G. Petretto, N. A. Pike, V. Planes, et al., *J. Chem. Phys.* **2020**, *152*, 124102.
[60] X. Gonze, B. Amadon, G. Antonius, F. Arnardi, L. Baguet, J.-M. Beuken, J. Bieder, F. Bottin, J. Bouchet, E. Bousquet, N. Brouwer, F. Bruneval, G. Brunin, T. Cavignac, J.-B. Charraud, W. Chen, M. Côté, S. Cottenier, J. Denier, G. Geneste, P. Ghosez, M. Giantomassi, Y. Gillet, O. Gingras, D. R. Hamann, G. Hautier, X. He, N. Helbig, N. Holzwarth, Y. Jia, et al., *Comput. Phys. Commun.* **2020**, *248*, 107042.
[61] X. Gonze, F. Jollet, F. A. Araujo, D. Adams, B. Amadon, T. Applencourt, C. Audouze, J.-M. Beuken, J. Bieder, A. Bokhanchuk, E. Bousquet, F. Bruneval, D. Caliste, M. Côté, F. Dahm, F. Da Pieve, M. Delaveau, M. Di Gennaro, B. Dorado, C. Espejo, G. Geneste, L. Genovese, A. Gerossier, M. Giantomassi, Y. Gillet, D. R. Hamann, L. He, G. Jomard, J. L. Janssen, S. Le Roux, et al., *Comput. Phys. Commun.* **2016**, *205*, 106.
[62] M. J. van Setten, M. Giantomassi, E. Bousquet, M. J. Verstraete, D. R. Hamann, X. Gonze, G.-M. Rignanese, *Comput. Phys. Commun.* **2018**, *226*, 39.
[63] D. R. Hamann, *Phys. Rev. B* **2013**, *88*, 085117.
[64] J. P. Perdew, M. Ernzerhof, K. Burke, *J. Chem. Phys.* **1996**, *105*, 9982.
[65] J. P. Perdew, K. Burke, M. Ernzerhof, *Phys. Rev. Lett.* **1996**, *77*, 3865.
[66] J. D. Pack, H. J. Monkhorst, *Phys. Rev. B* **1977**, *16*, 1748.
[67] H. J. Monkhorst, J. D. Pack, *Phys. Rev. B* **1976**, *13*, 5188.
[68] J. P. Perdew, Y. Wang, *Phys. Rev. B* **1992**, *45*, 13244.
[69] G. Kresse, D. Joubert, *Phys. Rev. B* **1999**, *59*, 1758.
[70] G. Kresse, J. Furthmüller, *Phys. Rev. B* **1996**, *54*, 11169.
[71] G. Kresse, J. Furthmüller, *Comput. Mater. Sci.* **1996**, *6*, 15.
[72] G. Kresse, J. Hafner, *Phys. Rev. B* **1993**, *47*, 558.
[73] P. E. Blöchl, *Phys. Rev. B* **1994**, *50*, 17953.
[74] T. E. Smidt, S. A. Mack, S. E. Reyes-Lillo, A. Jain, J. B. Neaton, *Sci. Data* **2020**, *7*, 72.
[75] Y. L. Li, L. E. Cross, L. Q. Chen, *J. Appl. Phys.* **2005**, *98*, 064101.
[76] M. J. Haun, E. Furman, S. J. Jang, H. A. McKinstry, L. E. Cross, *J. Appl. Phys.* **1987**, *62*, 3331.
[77] H. N. Lee, S. M. Nakhmanson, M. F. Chisholm, H. M. Christen, K. M. Rabe, D. Vanderbilt, *Phys. Rev. Lett.* **2007**, *98*, 217602.
[78] T. Le, O. Kurt, J. Ouyang, J. Wang, L.-Q. Chen, E. L. Lin, J. G. Ekerdt, Y. Ren, *Scr. Mater.* **2020**, *178*, 489.
[79] M. J. Weber, *Handbook of Optical Materials*, CRC Press, Boca Raton, FL, USA **2018**.
[80] H. Uwe, T. Sakudo, *J. Phys. Soc. Jpn.* **1975**, *38*, 183.
[81] I. C. Infante, S. Lisenkov, B. Dupé, M. Bibes, S. Fusil, E. Jacquet, G. Geneste, S. Petit, A. Courtial, J. Juraszek, L. Bellaiche, A. Barthélémy, B. Dkhil, *Phys. Rev. Lett.* **2010**, *105*, 057601.